

Cite this: *Nanoscale Adv.*, 2020, 2, 2577

A hierarchical SnS@ZnIn₂S₄ marigold flower-like 2D nano-heterostructure as an efficient photocatalyst for sunlight-driven hydrogen generation†

Aarti R. Gunjal,^{ab} Aniruddha K. Kulkarni,^b Ujjwala V. Kawade,^a Yogesh A. Sethi,^a Ravindra S. Sonawane,^{id}^a Jin Ook-Baeg,^{id}^c Arvind V. Nagawade^{*b} and Bharat B. Kale^{id}^{*a}

Herein, we report the *in situ* single-step hydrothermal synthesis of hierarchical 2D SnS@ZnIn₂S₄ nano-heterostructures and the examination of their photocatalytic activity towards hydrogen generation from H₂S and water under sunlight. The photoactive sulfides rationally integrate *via* strong electrostatic interactions between ZnIn₂S₄ and SnS with two-dimensional ultrathin subunits, *i.e.* nanopetals. The morphological study of nano-heterostructures revealed that the hierarchical marigold flower-like structure is self-assembled *via* the nanopetals of ZnIn₂S₄ with few layers of SnS nanopetals. Surprisingly, it also showed that the SnS nanopetals with a thickness of ~25 nm couple *in situ* with the nanopetals of ZnIn₂S₄ with a thickness of ~25 nm to form a marigold flower-like assembly with intimate contact. Considering the unique band gap (2.0–2.4 eV) of this SnS@ZnIn₂S₄, photocatalytic hydrogen generation from water and H₂S was performed under sunlight. SnS@ZnIn₂S₄ exhibits enhanced hydrogen evolution, *i.e.* 650 μmol h⁻¹ g⁻¹ from water and 6429 μmol h⁻¹ g⁻¹ from H₂S, which is much higher compared to that of pure ZnIn₂S₄ and SnS. More significantly, the enhancement in hydrogen generation is 1.6–2 times more for H₂S splitting and 6 times more for water splitting. SnS@ZnIn₂S₄ forms type I band alignment, which accelerates charge separation during the surface reaction. Additionally, this has been provoked by the nanostructuring of the materials. Due to the nano-heterostructure with hierarchical morphology, the surface defects increased which ultimately suppresses the recombination of the electron-hole pair. The above-mentioned facts demonstrate a significant improvement in the interface electron transfer kinetics due to such a unique 2D nano-heterostructure semiconductor which is responsible for a higher photocatalytic activity.

Received 1st March 2020
Accepted 16th April 2020

DOI: 10.1039/d0na00175a

rsc.li/nanoscale-advances

1. Introduction

Due to rapid fossil fuel consumption, increasing energy demands because of modern civilization growth, global warming, and the greenhouse effect, there have been serious challenges posed to the scientific community worldwide in the 21st century.^{1,2} Among all potential solutions being considered, hydrogen (H₂) is one of the promising candidates for green energy owing to its high energy density, non-polluting nature, easy transportability and zero hazardous gas emission.³ Hydrogen generation from water and H₂S splitting using solar

energy has attracted considerable attention for sustainable and renewable energy research.^{4,5} It is a crucial time that highly proficient, durable, eco-friendly and low-cost alternative energy production is a significant goal to solve energy and environmental problems. In this context, semiconductor-based photocatalytic H₂ generation from water splitting under sunlight is a promising technology for future fuel.^{6,7}

Sunlight-mediated hydrogen evolution from water splitting (solar energy to chemical fuel) by breaking of chemical bonds, similar to photosynthesis, *i.e.* (HER) (HER: 2H⁺ + 2e⁻ → H₂), required large Gibb's free energy change, *i.e.* 273 kJ mol⁻¹, which has to be supplied to initiate the reaction.⁸ This can be made possible using a narrow band gap semiconductor that absorbs maximum light upon exposure to sunlight. However, to meet the ideal criteria, semiconductors must satisfy several principal requirements. These include good solar light absorption capability, adequate band gap and band edge position with sufficient driving potential, efficient charge transfer kinetics, surface catalytic proton reduction potential, and minimal photo corrosion.^{9,10} The pioneering discovery was done

^aNanocrystalline Laboratory, Centre for Material for Electronic Technology (CMET), Department of Information Technology, Govt. of India, Panchawati, Off Pashan Road, Pune 411007, India. E-mail: bbkale1@gmail.com; bbkale@cmet.gov.in; Fax: +91 20 2589 8180; Tel: +91 20 2589 9273

^bDr John Barnabas Post-graduate School for Biological Studies, Ahmednagar College, Ahmednagar, India. E-mail: avnagawade@gmail.com

^cKorean Research Institute of Chemical Technology, 305-600, South Korea

† Electronic supplementary information (ESI) available. See DOI: 10.1039/d0na00175a



by Fujishima and Honda using a TiO_2 electrode for hydrogen generation.¹¹ Similar to TiO_2 , several alternative binary metal oxide photocatalysts such as Nb_2O_5 ,¹² Ta_2O_5 ,¹³ and ZnO ¹⁴ were developed and examined for hydrogen generation. However, their photocatalytic activity is not good enough for commercial purposes, due to low conductance, unsuitable indirect band gap, inadequate wide band gap range of light absorption and insufficient charge separation that leads to a rapid charge carrier's recombination process, with concomitant diminishing of their photocatalytic activity.¹⁵ To overcome these limitations, previous reports have shown that anion doping in TiO_2 catalysts tunes the band gap in the visible region, to improve the photocatalytic activity,¹⁶ but doping sites act as recombination centers which retard the photocatalytic activity. Some reports also showed that loading of noble metals such as Ag, Au, Pt, and Rh or co-catalysts on the surface of the passive oxide semiconductor enhances absorption towards longer wavelengths, but the widespread use of noble metals is not economically feasible.¹⁷

Recently, 2D transition metal dichalcogenides (TMDs), typical II–III₂–VI₄ semiconductors, are a large family of layered materials that have gained extensive interest due to their unique physicochemical properties and promising applications. 2D TMDs compared with 3D transition metal oxides possess a narrow band gap (1.23–3.0 eV), having a high specific surface area, and they can significantly inhibit charge carrier recombination; therefore, they have great potential for solar-light harvesting.^{18,19} To date, various 2D chalcogenides such as CdS ,²⁰ MoS_2 ,²¹ In_2S_3 ,²² ZnS ,²³ and ZnSe ,²⁴ have been reported and studied for good photocatalytic activity. However, these sulfides are having stability issues along with that photo-corrosion problem. To solve photo-corrosion problems, ternary sulfides such as CdIn_2S_4 ,²⁵ ZnIn_2S_4 ,²⁶ and CdMoS_4 (ref. 27) have been explored for improved stability and enhanced photocatalytic activity. Among all the reported ternary sulfides, ZnIn_2S_4 is a layered structure that has been proved to be a prominent visible light active catalyst due to its suitable band gap (2.3–2.5 eV) and excellent photocatalytic activity with stability.²⁸ In the past, various attempts have been made to enhance the photocatalytic activity of ZnIn_2S_4 , more specifically coupling of two individual semiconductors such as $\text{ZnIn}_2\text{S}_4/\text{TiO}_2$,²⁹ $\text{ZnIn}_2\text{S}_4/\text{CdS}$,³⁰ and $\text{ZnIn}_2\text{S}_4/\text{ZnFe}_2\text{S}_4$.³¹ With this motivation, we prepared a new $\text{SnS}@ZnIn_2S_4$ hybrid semiconductor by coupling ZnIn_2S_4 and SnS . The main aim of this semiconductor is to promote an interparticle electron transfer mediator to obtain two-step excitations, known as Z-scheme electron transfer. To the best of our knowledge, no previous work has reported on 3D hierarchical ZnIn_2S_4 coupled with SnS for photocatalytic application study. In this context, we successfully fabricated *in situ* $\text{SnS}@ZnIn_2S_4$ nanocomposite heterostructure photocatalysts by a facile hydrothermal method. The strong electrostatic interaction between negatively charged SnS and positively charged Zn and In ions of ZnIn_2S_4 facilitates close contact between ZnIn_2S_4 and SnS . Moreover, type I band alignment is designed in 2D ultrathin ZnIn_2S_4 and SnS , which provides highly efficient charge separation. The SnS provides active sites and acts as a co-catalyst for hydrogen generation.

In this work, we synthesized a $\text{SnS}@ZnIn_2S_4$ heterostructure photocatalyst and examined it for hydrogen generation under natural solar-light irradiation. It was found that $\text{SnS}@ZnIn_2S_4$ exhibits significantly enhanced photocatalytic activity for hydrogen evolution. Furthermore, the synergy between ZnIn_2S_4 and SnS and the possible mechanism underlying improved photocatalytic activity were studied systematically.

2. Experimental section

Zinc nitrate hexahydrate ($\text{Zn}(\text{NO}_3)_2 \cdot 6\text{H}_2\text{O}$), indium nitrate ($\text{In}(\text{NO}_3)_3 \cdot 4\text{H}_2\text{O}$), tin chloride dihydrate ($\text{SnCl}_2 \cdot 2\text{H}_2\text{O}$) and thiourea ($\text{N}_2\text{H}_4\text{CS}$) used for the preparation of catalysts were of analytical grade (SD-Fine-Chem Limited, India) and used without further purification.

2.1 Synthesis of ZnIn_2S_4 and $\text{SnS}@ZnIn_2S_4$

All the chemicals used for the synthesis of $\text{SnS}@ZnIn_2S_4$ were of analytical grade and used without further purification. $\text{SnS}@ZnIn_2S_4$ photocatalysts were synthesized by a hydrothermal method, and the procedure is briefly described as follows: first, 1 mole of zinc nitrate hexahydrate ($\text{Zn}(\text{NO}_3)_2 \cdot 6\text{H}_2\text{O}$) (99.99%) and 2 moles of indium nitrate ($\text{In}(\text{NO}_3)_3 \cdot 4\text{H}_2\text{O}$) (99.99%) were mixed in 50 mL water in a beaker (a). Similarly, 1 wt% tin chloride solution was prepared in 10 mL double-distilled water in another beaker (b) and added to the above mixture (a). The clear solution was then transferred to a 200 mL Teflon autoclave and kept at 160 °C for 30 h in an electric oven. As the synthesized catalyst was washed several times with absolute ethanol and deionized water, a yellow-colored powder was obtained. This samples were marked as S1 for pure ZnIn_2S_4 , S2 1% $\text{SnS}@ZnIn_2S_4$, S3 2% $\text{SnS}@ZnIn_2S_4$, and S4 3% $\text{SnS}@ZnIn_2S_4$ and used for further analyses and comparison thereafter. Similarly, different concentrations of tin chloride solution, namely, 1 wt%, 2 wt%, and 3 wt% respectively, were prepared, and the same procedure as mentioned above was followed to synthesize other samples. Hence, four samples were prepared for comparative purposes and each sample so obtained is represented and labeled as S1 for ZnIn_2S_4 , and 1% $\text{SnS}@ZnIn_2S_4$, 2% $\text{SnS}@ZnIn_2S_4$, 3% $\text{SnS}@ZnIn_2S_4$ as S2, S3, and S4, respectively, for convenience.

2.2 Photocatalytic study

2.2.1 Photocatalytic hydrogen generation from water. The photochemical reaction was carried out in a 70 mL total volume air-tight cylindrical quartz reactor with a cooling jacket for water circulation. All the reactions were carried out under ambient conditions with natural sunlight on sunny days (March to May months) between 10 am to 3 pm at Pune, located in the Maharashtra state of India. The intensity of solar light was measured using a digital Lux meter. The measured average intensity of solar light reaching the surface of the earth was 145 000 Lux. In a typical photocatalytic experiment, 15 mg of the photocatalyst was dispersed in 25 mL total volume containing 20% methanol (v/v) in aqueous solution. The free space only of photoreactor made airtight with rubber septum followed by



ultrasonication for 5 min for the uniform dispersion of catalyst. The solution mixture was then purged with ultra-high-purity nitrogen gas (UHP-99.999%) to remove all the gases in the headspace of the reactor and dissolved oxygen from the reaction mixture. Before and after irradiation with solar light, the gas in the free space of the reactor was analyzed by gas chromatography (GC). The generated gas was analyzed immediately by GC with a specific time interval.

2.3 Sample characterization

The phase formation and crystallite size of all synthesized samples were estimated using an X-ray diffractometer (XRD-D8, Advance, Bruker-AXS) with Ni-filtered Cu-K α radiation ($\lambda = 1.5418 \text{ \AA}$). The optical properties of the bare and Au-loaded samples were studied using a UV-vis-DRS spectrophotometer (UV 2600 spectrometer, Lambda-950, PerkinElmer) in the spectral range of 200–800 nm. The surface morphology was characterized using a field emission scanning electron microscope (FESEM; Hitachi, S-4800 II) and a field emission transmission electron microscope (FETEM; JEM-2000 FS). Image processing and interplanar distance (d) evaluation were performed using the micrograph Gatan software. The Brunauer–Emmett–Teller (BET) technique was employed to calculate the surface area from the adsorption branch (NOVA Touch, surface area and pore size analyzer, Quanta chrome instrument). Surface characterization of all SnS@ZnIn₂S₄ samples was carried out using a X-ray photoelectron spectrometer (XPS, ESCA-3000, VG Scientific Ltd.) at a pressure of $>1 \times 10^{-9}$ Torr. The general scan C 1s, S 2p, In 3d, Sn 3d, and Zn 2p core level spectra were recorded with non-monochromatized Mg-K α radiation (photon energy – 1253.6 eV). Baseline correction and peak fitting for all the samples were performed using the software package XPS peak-41. The core-level binding energies (BEs) were aligned with respect to the C 1s binding energy of 285 eV. The collected gas sample was analyzed using a gas chromatography system (Shimadzu GC-2014) with a portapak-Q packed column coupled with a TCD detector and nitrogen (N₂-UHP) as a carrier gas.

3. Results and discussion

3.1 Structural study

A facile low-temperature one-step hydrothermal method was employed for the *in situ* preparation of SnS@ZnIn₂S₄ nano-heterostructures. Fig. 1 (S1–S4) shows powder X-ray diffraction patterns of the as-prepared ZnIn₂S₄ and SnS@ZnIn₂S₄ nano-composites. Fig. 1 (S1) and (S2–S4) shows the X-ray diffraction patterns of pure ZnIn₂S₄ and SnS@ZnIn₂S₄. Major diffraction peaks located at 2θ values 21.5, 27.6 and 47.1° could be attributed to the reflection of the (0 0 6) (1 0 2) and (1 1 0) planes of hexagonal ZnIn₂S₄ which matches well with JCPDS card no-01-072-0773.³² Fig. 1 (S2–S4) shows the XRD pattern of SnS@ZnIn₂S₄ samples in which additional peaks are observed with the co-existence of both ZnIn₂S₄ and SnS phases. The major diffraction peaks located at 2θ values 22.0, 30.4, 34.5, 39.0 and 53.4° could be attributed to the reflection of the (0 0 1) (0



Fig. 1 X-ray diffraction patterns of (S1) pure ZnIn₂S₄, (S2) 1% SnS@ZnIn₂S₄, (S3) 2% SnS@ZnIn₂S₄ and (S4) 3% SnS@ZnIn₂S₄ sample photocatalysts.

0 1) (2 1 1) (3 1 1) and (6 0 1) planes of orthorhombic SnS³³ (JCPDF card no-01-073-1859), demonstrating the successful formation of the SnS@ZnIn₂S₄ composite material. The XRD pattern of pure SnS is shown in ESI (Fig. I).[†] Impurity peaks of binary sulfides such as ZnS and In₂S₃ could not be observed, which confirms the phase purity of the as-prepared samples. Although SnS has a great influence on the surface morphology of ZnIn₂S₄, it does not affect the crystal structure of ZnIn₂S₄. Furthermore, it is observed that the diffraction peak intensity and crystallinity of both SnS and ZnIn₂S₄ increase with the increase in the content of SnS from (S2–S4). Besides, the relative intensity of the (1 0 4) plane increases with the increase in the concentration of SnS and diminished the relative intensity of the (0 0 6) plane of ZnIn₂S₄. It is evident that no significant shift in the peak positions was observed in each as-synthesized SnS@ZnIn₂S₄ sample, signifying that the deposited SnS is not incorporated into the lattice of ZnIn₂S₄.

3.2 Surface and morphological studies

Fig. 2 shows a representative FE-SEM image of pure ZnIn₂S₄ and SnS@ZnIn₂S₄ nano-heterostructures. Fig. 2(a and b) shows the morphology of pure ZnIn₂S₄, in which the uniform marigold flower-like structure of ZnIn₂S₄ (3–5 μm) comprised the self-



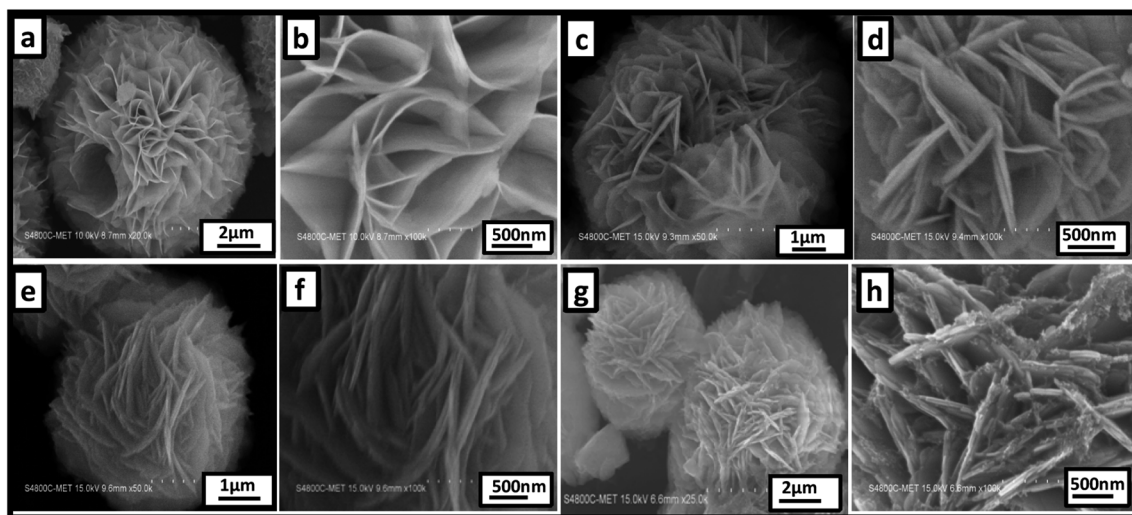


Fig. 2 Representative FE-SEM images of (a and b) pure ZnIn_2S_4 , (c and d) 1% $\text{SnS}@ZnIn_2S_4$, (e and f) 2% $\text{SnS}@ZnIn_2S_4$ and (g and h) 3% $\text{SnS}@ZnIn_2S_4$ sample photocatalysts.

assembly of nanopetals under hydrothermal conditions. Surprisingly, the diameter of the petals is in the micron range; however, the thickness of the petal is few nanometers, *i.e.* ~ 25 nm. The aspect ratio of one petal is more than 500 nm, which clearly shows the enhanced surface area of a single flower. Fig. 2(c and d) shows the surface morphology of 1% SnS-loaded ZnIn_2S_4 , in which the marigold flower-like structure (2.4–5 μm) is composed of nanopetals of SnS and ZnIn_2S_4 . The thickness of the twin nanopetals is measured to be 20–25 nm, and it is around 50 nm for coupled nanopetals of the nano-heterostructure. We can see the parallel growth of SnS and ZnIn_2S_4 petals in composed marigold flower-like structures (Fig. 2(d)). The growth of the flowers has been accelerated with SnS. The growth orientation has been changed significantly with the increase in the content of SnS, as shown in Fig. 2(e and f) (2–5 μm). The surface morphology of 2% loaded SnS on ZnIn_2S_4 clearly shows a porous marigold flower-like structure assembled with thin petals of SnS and ZnIn_2S_4 .

The length of the nanopetals is in the range of 500–1000 nm, and the thickness is measured to be 50 nm. Significantly, here also we can see the twin petals, *i.e.* SnS and ZnIn_2S_4 . Fig. 2(f) shows a thickness of 25 nm for each of the petals. Fig. 2(g and h) shows the morphology of 3% SnS-loaded ZnIn_2S_4 , which shows distorted flowers (2–7 μm). Furthermore, it was observed that these flowers are made up of thick (50 nm) SnS and ZnIn_2S_4 nanopetals along with a cluster of SnS (5–10 nm) nanoparticles.

Furthermore, FE-TEM investigations (as shown in Fig. 3(a–d)) were performed to determine the morphology and crystalline nature of the $\text{SnS}@ZnIn_2S_4$ nano-heterostructure. Fig. 3(a and b) shows the TEM images of the $\text{SnS}@ZnIn_2S_4$ nanopetals with an ordered uniform structure. The ultrathin ZnIn_2S_4 nanopetals are coupled with nanopetals of SnS, and they form a $\text{SnS}@ZnIn_2S_4$ nano-heterostructure, which is in good agreement with the XRD data. Significantly, very thin petals of ZnIn_2S_4 and SnS of a few nanometer thickness were observed. Fig. 3(c) shows the HRTEM images of $\text{SnS}@ZnIn_2S_4$ taken at the

edge part, which depicts a lattice spacing of 0.318 nm that could be assigned to the (1 0 2) plane of hexagonal ZnIn_2S_4 and 0.284 nm assigned to the (1 1 1) plane of SnS matching with the XRD results. The selected area electron diffraction (SAED) pattern shown in Fig. 3(d) indicates the as-synthesized $\text{SnS}@ZnIn_2S_4$ nanocomposite of crystalline nature. Fig. 3(e) shows the EDAX spectra that confirm the co-existence of Zn, In, Sn and S elements. Furthermore, Fig. 3(f) also shows the STEM elemental mapping, which confirms the existence of Zn, In, Sn and S. The corresponding elemental mapping of Zn, In, S and Sn are identical with each other, which illustrates the attractive porous nature. Hence, it is reasonable to believe that the 2D $\text{SnS}@ZnIn_2S_4$ heterostructure with intimate interfacial contact also shows synergy between SnS and ZnIn_2S_4 micropetals.

Furthermore, nitrogen (N_2) adsorption–desorption experiments were performed in order to study the textural properties of the as-synthesized ZnIn_2S_4 and SnS loaded ZnIn_2S_4 nanocomposites. The N_2 adsorption–desorption isotherms of ZnIn_2S_4 (S1) and $\text{SnS}@ZnIn_2S_4$ (S3) at 77 K and their textural property values were measured, and they are given in ESI Table 1.† Both structures exhibit type IV isotherm, which clearly reveals the mesoporous nature with a H3-type hysteresis loop, indicating the aggregation of ZnIn_2S_4 nanopetals forming slit-like pores, as shown in ESI, Fig. II.† The pore size and pore volume were obtained from the BJH desorption curve, which shows a pore radius of 7.5 nm with a volume of $0.28 \text{ cm}^3 \text{ g}^{-1}$ for pure ZnIn_2S_4 (S1). A pore radius of 5.1 nm with a pore volume of 0.18 cc/g was observed for 2% SnS loaded on ZnIn_2S_4 (S3). The specific surface area obtained from the desorption study for sample S1 is observed to be $74.3 \text{ m}^2 \text{ g}^{-1}$ and for sample S3, it is $78.3 \text{ m}^2 \text{ g}^{-1}$. From the BET study, it is clear that with the increase in SnS contents, the specific surface area slightly increases but the pore size and pore volume decrease significantly.

Furthermore, the formation mechanism is schematically depicted in Scheme 1. The hydrothermal reaction conditions



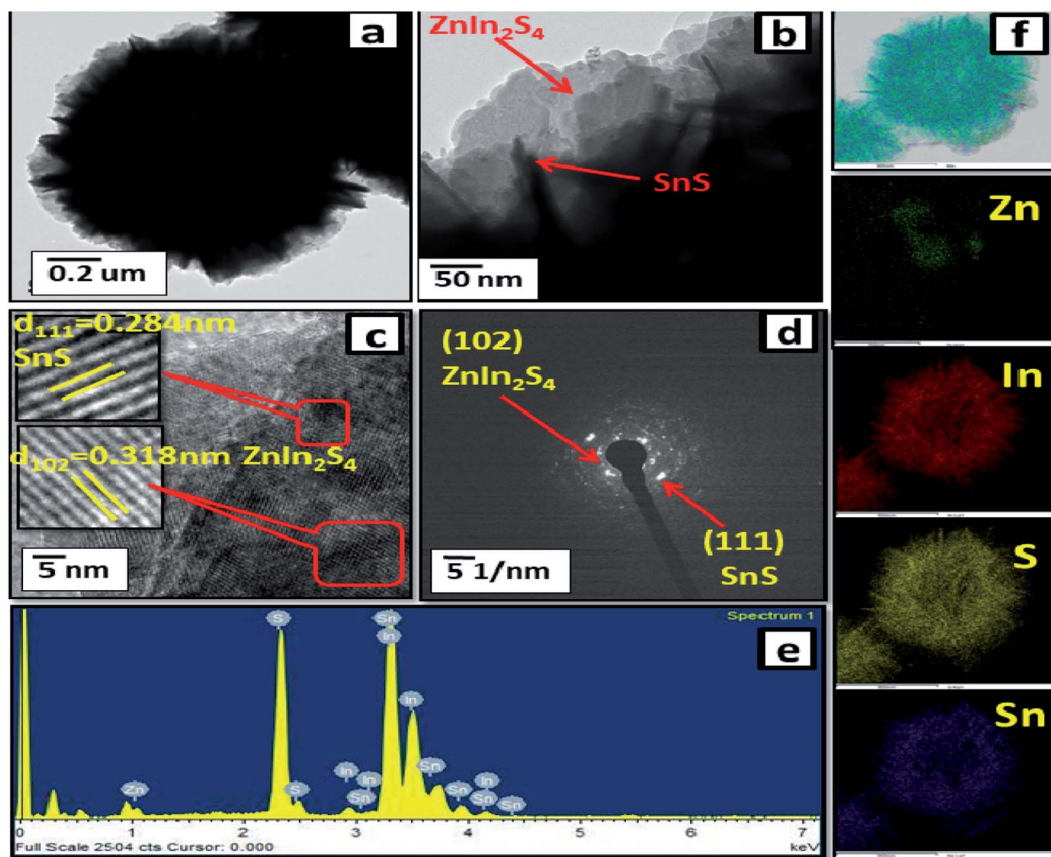
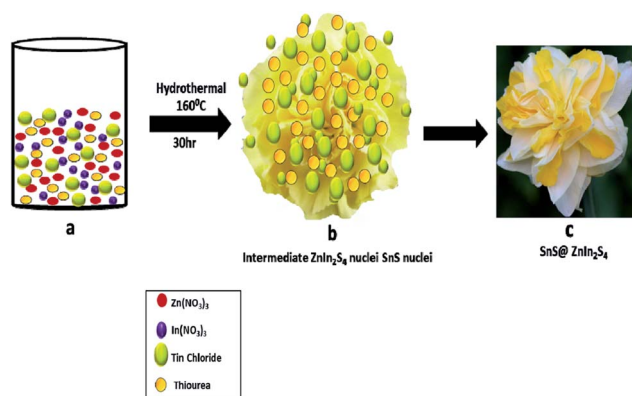
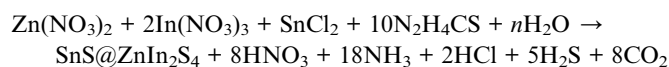


Fig. 3 FE-TEM images (a and b), (c) HRTEM image, (d) SAED pattern, (e) EDAX spectra and (f) elemental mapping of 2% SnS-loaded ZnIn₂S₄.



Scheme 1 Schematic of the formation mechanism of SnS@ZnIn₂S₄ nano-heterostructures.

are well known to obtain different morphologies. In the present case, the reaction between precursor salt solutions and thiourea confirmed the formation of ZnIn₂S₄ nuclei under hydrothermal conditions. Thiourea is water-soluble and stable at room temperature, and as the temperature increased, it got decomposed and formed H₂S and NH₂CN. Then, NH₂CN reacted with water at 160 °C and released NH₃ and CO₂ gas. The overall reaction is shown as follows:³⁴



The Zn²⁺ In³⁺ and Sn²⁺ cations easily get attracted to S²⁻ anions in an aqueous solution of thiourea. Zn(NO₃)₂ and In(NO₃)₃ have a very high degree of ionization in the aqueous medium due to its polarity.³⁵ In an aqueous solution of thiourea, the ZnIn₂S₄ petals slowly with prolonged reaction time. The nascent ZnIn₂S₄ is unstable due to its high surface energy; to reduce these energies, they get aggregated due to the van der Waals force of attraction between small crystallites. Finally, the 2D growth of nanoparticles takes place, which self-assembled to form a hierarchical marigold flower-like structure. The growth of SnS is very slow because of the low concentration of Sn precursors in the reaction. During the hydrothermal reaction, the growth of ZnIn₂S₄ is fast as compared to SnS. Hence, SnS nanopetals decorated on the surface of ZnIn₂S₄, which is in good agreement with the FE-TEM images. The above-discussed mechanism is based on our experimental evidence. Such unique twin marigold flower-like nanostructures were reported for the first time.

3.3 Optical and electronic studies

A good solar light absorption capability is a key requirement for highly efficient semiconductor photocatalysts. The absorption properties of pure ZnIn₂S₄ and SnS@ZnIn₂S₄ nano-



heterostructures were studied by UV-DRS spectra. Fig. 4(a) shows the UV-visible spectrum of ZnIn_2S_4 and SnS-loaded ZnIn_2S_4 heterostructures in different molar ratios. The absorption edge of pure ZnIn_2S_4 is observed to be 600 nm (2.0 eV). The absorption edge of pure SnS is shown in ESI, Fig. III.† The dual band gap is observed for SnS@ ZnIn_2S_4 samples S2–S4.³⁶ Sample S2 and S3 show absorption edges at 610 nm (2.03 eV) and 640 nm (1.7 eV), which correspond to ZnIn_2S_4 and SnS, respectively. Furthermore, the sample S4 shows an absorption edge at 560 nm (2.21 eV) and 600 nm (2.1 eV), which might be due to ZnIn_2S_4 and SnS respectively. The reduction in the band gap is an indication of a very intimate interaction between SnS and ZnIn_2S_4 nanopetals. The first absorption edge found at 516 nm (2.4 eV) is predominant. The increase in band gap clearly reveals the close interaction between ZnIn_2S_4 flowers and SnS thin sheets. The change in band gap clearly signifies the effect of SnS on ZnIn_2S_4 . As the amount of SnS increases in the composites, the absorption is strongly dominated by SnS present in it. There is a slight shift in the absorption edges to the lower wavelength observed with the increasing SnS concentration; it is due to a lower particle size of the material.

Photoluminescence (PL) spectra is a unique property to evaluate the generation, transfer and separation processes of the photo-induced electrons and hole.³⁷ Fig. 5 shows a comparative study of the PL spectra of pure ZnIn_2S_4 and SnS@ ZnIn_2S_4 excited at a wavelength of 400 nm at room temperature. The PL study of pure SnS is shown in ESI, Fig. IV.† The high PL intensity shows rapid electron–hole pair recombination in a photocatalyst. The pure ZnIn_2S_4 has strong emission peak at about 590 nm, which is assigned to the origin from the band gap energies transition of ZnIn_2S_4 .³⁸ The PL spectrum of the S2–S4 heterostructure shows the presence of two emission peaks at 530 and 590 nm, which highlights the association of SnS and ZnIn_2S_4 . The PL intensity of SnS@ ZnIn_2S_4 significantly declined with the increase in the content of the SnS sample (S2 and S3), as compared to pure ZnIn_2S_4 . The significant decline in intensity is due to either the faster migration process with the shorter lifetime or the slower recombination process with the

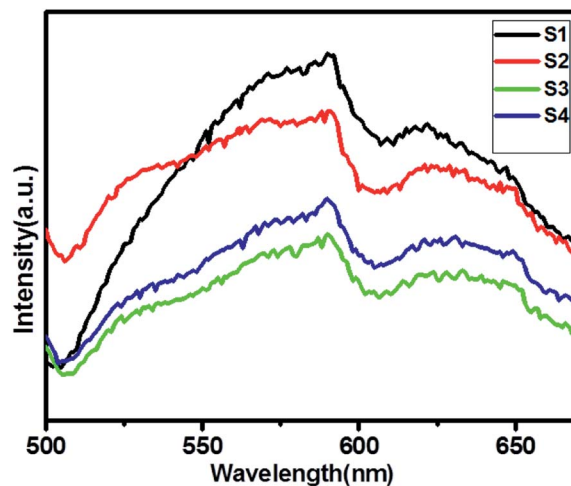


Fig. 5 UV-DRS spectra of (S1) pure ZnIn_2S_4 , (S2) 1% SnS@ ZnIn_2S_4 , (S3) 2% SnS@ ZnIn_2S_4 and (S4) 3% SnS@ ZnIn_2S_4 sample photocatalysts.

longer lifetime for the photo-induced electrons and holes at the interface of two semiconductors as compared to the individual components of the SnS@ ZnIn_2S_4 nano-heterostructure. The incorporation of SnS creates the sulfur vacancy defects, which ultimately reduce the intensity of emission peaks in SnS@ ZnIn_2S_4 . Furthermore, high concentrations of SnS (3%) increase the recombination rate due to the shielding of incident light that prevents the generation of electrons inside the ZnIn_2S_4 nanopetals. Hence, an optimum amount of SnS, *i.e.* 2% SnS, suppresses the recombination rate. The above-mentioned results reveal that the charge recombination in ZnIn_2S_4 is effectively suppressed with the increase in the amount of SnS, *i.e.* due to sulfur vacancy defects.^{39–41}

3.4 XPS study

The surface chemical composition and valence state of the SnS@ ZnIn_2S_4 architecture were investigated by X-ray photoelectron spectroscopy. All the peaks were calibrated using the C 1s reference peak at 284.6 eV. Fig. 6(a) shows the XPS signal of Zn 2p observed at binding energies around 1022.3 eV ($\text{Zn}^{2+} 2p_{3/2}$) and 1045.3 eV ($\text{Zn}^{2+} 2p_{1/2}$), which is consistent with the results reported in the previous literature.³⁰ Fig. 6(b) shows the high-resolution XPS spectra of In 3d at binding energies 444.8 ($\text{In}^{3+} 3d_{5/2}$) and 452.4 eV ($\text{In}^{3+} 3d_{3/2}$), which is in good agreement with the previous work.⁴² Furthermore, the XPS signal (Fig. 6(c)) observed at a binding energy of 161.7 eV is ascribed to the divalent sulfide ions ($\text{S}^{2-} 2p_{3/2}$) which is inconsistent with the data of ZnIn_2S_4 .⁴³ Fig. 6(d) shows high-resolution spectra of Sn 3d, where the region can be divided into two different peaks at 487.4 and 497.7 eV. This can be ascribed to the Sn $3d_{5/2}$ and $\text{Sn}_{3/2}$ levels of tin in the SnS products, which exist in +2 oxidation state.⁴⁴ Based on the above-mentioned results, it is evident that SnS nanopetals are overlapped on ZnIn_2S_4 . In comparison with reported binding energies of pure ZnIn_2S_4 , there is a shift in the binding energies of SnS@ ZnIn_2S_4 , indicating a strong interaction between ZnIn_2S_4 and SnS similar to the other reported

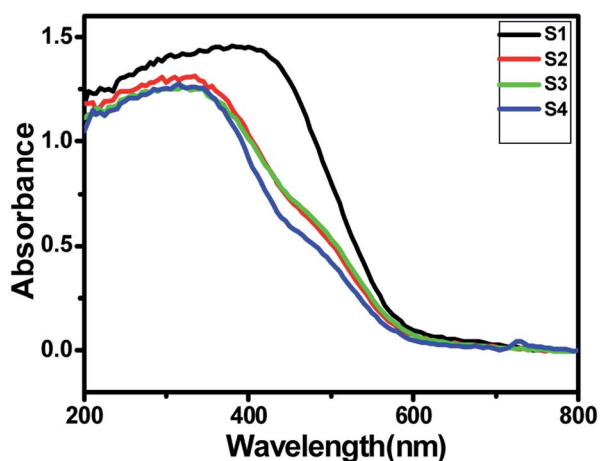


Fig. 4 UV-DRS spectra of (S1) pure ZnIn_2S_4 , (S2) 1% SnS@ ZnIn_2S_4 , (S3) 2% SnS@ ZnIn_2S_4 and (S4) 3% SnS@ ZnIn_2S_4 sample photocatalysts.



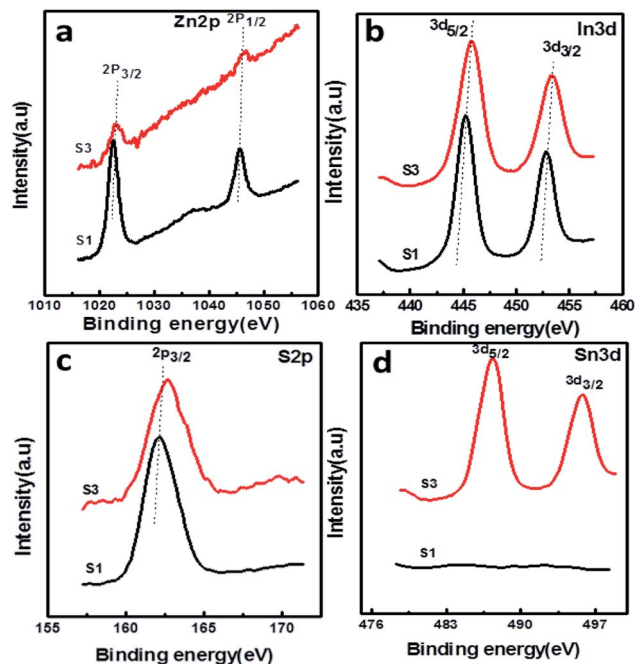


Fig. 6 XPS spectra of the as-prepared SnS@ZnIn₂S₄ nanocomposites: (a) Zn 2p, (b) In 3d, (c) S 2p, and (d) Sn 3d.

nano-heterostructures. This close interfacial contact facilitates electron transfer between SnS and ZnIn₂S₄ to achieve an equivalent position of the Fermi level of both the semiconductors. The optical properties also conclude that the synergic interaction among SnS and ZnIn₂S₄ matrices exhibits alteration in the electronic band structure of ZnIn₂S₄ and creates energy levels between C.B and V.B.³⁸

3.5 Photocatalytic study

3.5.1 Photocatalytic activity measurement. As conferred earlier, SnS@ZnIn₂S₄ is a good semiconductor having a narrow band gap falling in the visible region at room temperature. Considering the good response towards solar light, photocatalytic activities of SnS@ZnIn₂S₄ have been investigated. Herein, we report the photocatalytic H₂ evolution performance from water and H₂S under natural solar light irradiation.

3.5.2 Photocatalytic H₂ evolution from H₂O and H₂S splitting. The effect of SnS loading on ZnIn₂S₄ and their photocatalytic activity of hydrogen generation were studied under solar light irradiation using Na₂S/Na₂S₂O₃ as a scavenger electron donor.⁴⁵ A series of experiments were performed using different concentrations of SnS on the surface of ZnIn₂S₄, and their results are given in Table 1. The investigation results indicated that the maximum hydrogen generation, *i.e.* 650 μmol h⁻¹ g⁻¹, was obtained for the sample S3, whereas pure ZnIn₂S₄, and SnS shows hydrogen evolution rates of 80.2 and 115.5 μmol h⁻¹ g⁻¹. Furthermore, 1% SnS-decorated ZnIn₂S₄ and 3% SnS-decorated ZnIn₂S₄ give 386.3 and 290 μmol h⁻¹ g⁻¹ respectively. Fig. 7 shows the time-dependent hydrogen generation using the as-synthesized ZnIn₂S₄ and SnS@ZnIn₂S₄ nano-heterostructures. The linearity of the graph shows a continuous

Table 1 H₂ generation rates for the as-synthesized ZnIn₂S₄, SnS and SnS@ZnIn₂S₄ nanocomposites

Sr. no.	Sample code	H ₂ evolution rate from water (μmol h ⁻¹ g ⁻¹)	H ₂ evolution rate from H ₂ S (μmol h ⁻¹ g ⁻¹)
1	S0	80.2	3287
2	S1	115.5	4180
3	S2	386.3	5593
4	S3	650	6429
5	S4	290	5808

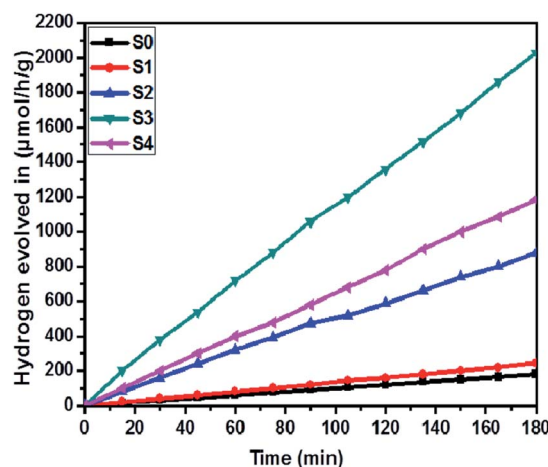
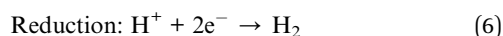
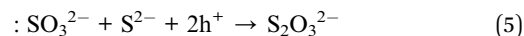
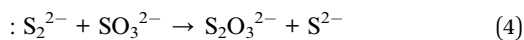
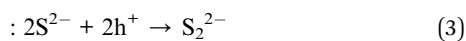
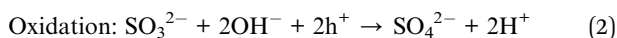
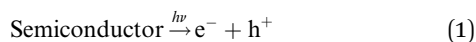


Fig. 7 Time versus volume of H₂ (μmol h⁻¹ g⁻¹) evolution from H₂O of all the samples synthesized at 160 °C for 30 h: (S0) pure SnS, (S1) pure ZnIn₂S₄ and SnS@ZnIn₂S₄ nano-heterostructures prepared with different percentages of SnS loading: (S2) 1%, (S3) 2% and (S4) 3%.

and stable hydrogen generation rate. However, the pure ZnIn₂S₄ shows poor hydrogen evolution, *i.e.* 115.5 μmol h⁻¹ g⁻¹, whereas maximum hydrogen production, *i.e.* 650 μmol h⁻¹ g⁻¹, was obtained for sample 2% SnS@ZnIn₂S₄ (S3) nano-heterostructure, which reveals that most exciting electrons are available for proton reduction. For this experiment, we used 70 mL DI water and Na₂S/Na₂S₂O₃ mixture as a sacrificial agent. In the present case, 0.25 M Na₂S and 0.35 M Na₂S₂O₃ mixture were used to resist the photo-corrosion of the semiconductor. Moreover, the Na₂S solution acts as a hole scavenger, and it oxidized S₂²⁻ into S²⁻, which is beneficial for hydrogen generation from SnS@ZnIn₂S₄ rather than alcohol. The photocatalytic hydrogen generation mechanism from water is well reported and discussed in the previous literature.³⁸ The semiconductor photocatalyst after interaction with solar light with energy greater than or equal to band gap energy generates electrons in CB and holes in VB. It causes redox reactions of adsorbed species on a semiconducting material. The photo-generated holes from VB irreversibly oxidize S₂²⁻, which was reduced back to S²⁻ by Na₂S₂O₃ and radially got adsorbed on the surface of semiconductor producing protons (H⁺) and free radicals, while electrons from CB reduce H⁺ ions into molecular hydrogen.⁴⁶





Furthermore, considering the good performance of hydrogen generation from water, we have also performed H_2S splitting under solar light irradiation. The photocatalytic hydrogen generation *via* decomposition of hydrogen sulfide (H_2S) was also carried out using the as-synthesized $\text{SnS}@Zn\text{In}_2\text{S}_4$ nano-heterostructure without any sacrificial reagents under solar light. Fig. 8 shows the time-dependent hydrogen generation rate from H_2S splitting using the as-synthesized $\text{SnS}@Zn\text{In}_2\text{S}_4$ nanocomposite. The photocatalytic hydrogen generation mechanism from H_2S is well reported and discussed in the previous literature.^{34,35} The pure SnS (S0) and ZnIn_2S_4 (S1) samples exhibit hydrogen evolution rates of 3287 and 4180 $\mu\text{mol h}^{-1} \text{g}^{-1}$ respectively, whereas, 1%, 2% and 3% SnS -loaded ZnIn_2S_4 (S2–S4) samples exhibit hydrogen evolution rates of 5593, 6429 and 5808 $\mu\text{mol h}^{-1} \text{g}^{-1}$ respectively. From experimental results, it is observed that the loading of SnS on ZnIn_2S_4 enhances the hydrogen generation efficiency compared with pure SnS and ZnIn_2S_4 . The highest hydrogen generation, *i.e.* 6429 $\mu\text{mol h}^{-1} \text{g}^{-1}$, was obtained using the 2% SnS -loaded ZnIn_2S_4 sample (S2). In both the cases, hydrogen evolution is higher than that reported in earlier studies (Table 2 ESI†).

It is exciting to discuss the improved photocatalytic activity in the present case. It is well reported that the photocatalytic

activity of semiconductors depends on the adequate band gap, crystallinity, hierarchical morphology, specific surface area, visible light absorption capability, diffusion rate of charge carriers and electronic structure.⁴⁷ Based on the experimental results, enhanced photocatalytic activity ascribed to the formation of heterostructures can be discussed using probable mechanisms. In the PL study, we observed that the intensity of the emission peaks decreases with the percentage of SnS . As discussed earlier, 2% $\text{SnS}@Zn\text{In}_2\text{S}_4$ (S3) shows minimum intensity as compared to others due to vacancy defects. This supports that the as-synthesized $\text{SnS}@Zn\text{In}_2\text{S}_4$ nanopetals are heterojunctions, which enhance the charge separation efficiency. Hence, the enhanced photocatalytic activity is due to effective charge separation by trapped hole formation in ZnIn_2S_4 and the transportation of electrons to SnS , *i.e.* slower the recombination process with longer lifetime for photo-assisted electrons and holes at the interface of two semiconductors compared with pristine ZnIn_2S_4 . Hence, in the present case, the SnS nanoplates loaded on the surface of ZnIn_2S_4 may act as an optical filter or co-catalyst for charge separation. Based on the experimental results, the band gaps of ZnIn_2S_4 and SnS are 2.03 and 1.7 eV, respectively. Therefore, both ZnIn_2S_4 and SnS can be excited and generate charge carriers under solar light irradiation. Furthermore, the band structure of $\text{SnS}@Zn\text{In}_2\text{S}_4$ has a stacked system with a metal-nonmetal bridged heterojunction exhibiting type I band alignment, which may be due to the reorganization of charge carriers at the interlayer region. The type I band alignment specifies that the excited charge carriers are confined to opposite layers, which facilitate the effective separation of electron-hole pairs, resulting in enhanced hydrogen generation.⁴⁰ Pure ZnIn_2S_4 shows low photocatalytic activity, but due to a well-matched overlapping band structure and intimate contact between SnS and ZnIn_2S_4 , the photogenerated electrons on the surface of SnS can be easily transferred to the CB of ZnIn_2S_4 . It is because the CB band edge potential of SnS is more negative than ZnIn_2S_4 , which results in the accumulation of more negative charges at the ZnIn_2S_4 region near the junction. Moreover, the holes on the VB of ZnIn_2S_4 could be transferred to the VB of SnS through the close contact junction.⁴⁸ It is because the VB band edge potential of ZnIn_2S_4 is more positive than that of SnS , which results in a more positive charge accumulated at the SnS region near the interface, which results in the production of an electric field (E) at the interface. The internal electric field migrates at the interface, which promotes the photoinduced charge carriers to participate in hydrogen generation. In other words, ZnIn_2S_4 can be excited using sunlight, and electron hole-pairs are simultaneously generated. However, the electrons and holes easily recombine without SnS .⁴⁹ The formation of $\text{SnS}@Zn\text{In}_2\text{S}_4$ has the synergistic effect between ZnIn_2S_4 and SnS which changes CB and VB of the ZnIn_2S_4 flower. It suppresses the recombination probability of charge carriers and making them available for photocatalytic activity. It is concluded that the $\text{SnS}@Zn\text{In}_2\text{S}_4$ heterostructure provides electrons and holes to the active sites of the catalyst and reduces the recombination rate. The 2% loading of SnS on ZnIn_2S_4 suppresses the charge carrier recombination rate significantly.⁵⁰ Furthermore, the co-

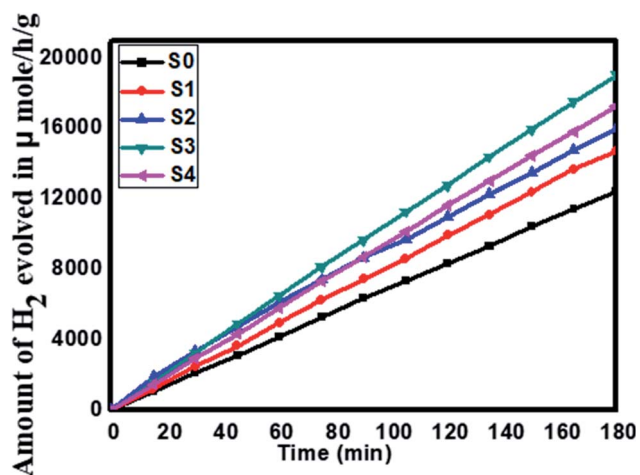


Fig. 8 Time versus volume of H_2 ($\mu\text{mol h}^{-1} \text{g}^{-1}$) evolution from H_2S of all the samples synthesized at 160 °C for 30 h: (S0) pure SnS , (S1) pure ZnIn_2S_4 and $\text{SnS}@Zn\text{In}_2\text{S}_4$ nano-heterostructures prepared with different percentages of SnS loading: (S2) 1%, (S3) 2%, and (S4) 3%.



existence of sulfur vacancies with optimized concentration can also trap electrons and provide more electrons for hydrogen generation. In addition, the ZnIn_2S_4 and SnS interface creates a super hydrophilic surface that can effectively improve the contact of semiconductor water, semiconductor H_2S , and bubble detachment. The lowering recombination of electron-hole can be correlated by considering the energy level diagram of $\text{SnS@ZnIn}_2\text{S}_4$ heterostructures. The CB of ZnIn_2S_4 can be shown at -0.84 eV, while VB would be located at 1.56 eV. The Fermi level of SnS -0.19 vs. NHE is more positive than the CB of ZnIn_2S_4 , which indicates that photogenerated electrons can transfer from CB of ZnIn_2S_4 to SnS (Scheme 2).^{34,51} Furthermore, with an increase in the concentration of SnS (3% SnS-loaded ZnIn_2S_4), the photocatalytic activity was found to decrease. It may be due to excessive concentration of SnS (more than 2%), which acts as a recombination center and covers the active sites on ZnIn_2S_4 . Moreover, at a higher concentration of SnS, there is a reduction in charge transfer taking place between SnS and ZnIn_2S_4 , which leads to higher charge recombination. Additionally, the PL study shows a drastic decline in the peak intensity, which also shows suppression in the charge carrier at an optimum concentration of SnS on ZnIn_2S_4 . Furthermore, for 3% of $\text{SnS@ZnIn}_2\text{S}_4$, the PL intensity increases slightly and shows an increase in the charge carrier recombination rate, which may be due to either the faster migration process with a shorter lifetime or the slower recombination process with a longer lifetime. Hence, higher activity is obtained at a moderate concentration of SnS, *i.e.* 2%. Overall, the $\text{SnS@ZnIn}_2\text{S}_4$ nano-heterostructure photocatalyst was found to be quite stable and active for hydrogen generation under solar light irradiation. A similar trend of hydrogen generation was observed *via* H_2S and water splitting. The H_2 production rate by H_2S splitting is more as compared to water because of the lower ΔG for H_2S splitting. Overall, sample S3 shows good photocatalytic activity under sunlight. To examine the stability of the catalysts, the experiments have been performed reusing the photocatalysts. We obtained a similar activity after reusing the

catalysts for 3 cycles (Fig. V and VI ESI†). It shows that the heterostructure is quite stable and can be used for many cycles.

4. Conclusion

In summary, highly efficient 2D $\text{SnS@ZnIn}_2\text{S}_4$ nano-heterostructure flowers have been designed by a hydrothermal method, in which SnS nanopetals decorated *in situ* on the surface of ZnIn_2S_4 nanopetals for the first time. An excellent photocatalytic hydrogen evolution rate of $6429 \mu\text{mol h}^{-1} \text{g}^{-1}$ was obtained for 2% $\text{SnS@ZnIn}_2\text{S}_4$, under solar light irradiation from H_2S , which is 1.6–2 times higher than that of pure ZnIn_2S_4 . At the same time, an excellent photocatalytic hydrogen evolution rate of $650 \mu\text{mol h}^{-1} \text{g}^{-1}$ was obtained by water splitting, which is 6 times higher than that of bare ZnIn_2S_4 . The enhanced photocatalytic activity of the $\text{SnS@ZnIn}_2\text{S}_4$ photocatalyst was ascribed to efficient charge separation and transportation of the photogenerated electron-hole pairs through the formation of “type I band alignment” at the interface and increase in the visible light response. More significantly, the hierarchical nanostructure of $\text{SnS@ZnIn}_2\text{S}_4$ enhances the photocatalytic activity due to the efficient charge carrier separation, which has been examined using the PL study. It also reveals a moderate amount of SnS incorporation that gives good photocatalytic activity. The reusability of the photocatalyst exhibits similar activities, which reveals the good stability of the catalyst.

Conflicts of interest

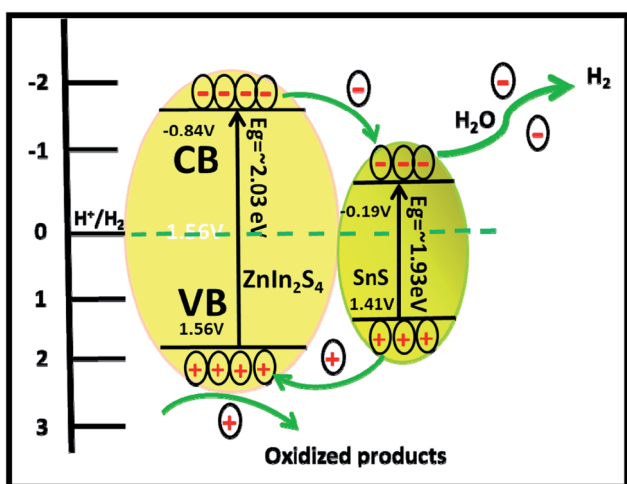
There are no conflicts to declare.

Acknowledgements

ARG and AKK would like to thanks Dr R. J. Barnabas (Principal Ahmednagar College Ahmednagar) for useful discussion and ASPIRE SPPU for financial support. The authors would like to thank Nanocrystalline Materials Group, C-MET, Pune and Ahmednagar College Ahmednagar, for the kind support. Dr Jin-Ook Baeg thanks to KRICT for support. BBK would like to thank the Ministry of Electronics and Information Technology (MeitY), Government of India for financial support and C-MET Pune for providing research facilities. ARG would like to acknowledge to SPPU Pune for Providing J. R. D. Tata fellowship for Research work.

References

- 1 F. E. Osterloh, *Chem. Mater.*, 2008, **20**, 35–54.
- 2 J. Zheng, H. Zhou, Y. Zou, R. Wang, Y. Lyu, S. P. Jiang and S. Wang, *Energy Environ. Sci.*, 2019, **12**, 2345–2374.
- 3 I. Staffell, D. Scamman, A. Velazquez Abad, P. Balcombe, P. E. Dodds, P. Ekins, N. Shah and K. R. Ward, *Energy Environ. Sci.*, 2019, **12**, 463–491.
- 4 A. K. Kulkarni, R. P. Panmand, Y. A. Sethi, S. R. Kadam, S. P. Tekale, G. H. Baeg, A. V. Ghule and B. B. Kale, *Int. J. Hydrogen Energy*, 2018, **43**, 19873–19884.
- 5 A. Kudo and Y. Miseki, *Chem. Soc. Rev.*, 2009, **38**, 253–278.



Scheme 2 Schematic of the photocatalytic mechanism of $\text{SnS@ZnIn}_2\text{S}_4$ heterostructures.



- 6 X. Chen, S. Shen, L. Guo and S. S. Mao, *Chem. Rev.*, 2010, **110**, 6503–6570.
- 7 R. K. Chava, J. Y. Do and M. Kang, *J. Mater. Chem. A*, 2019, **7**, 13614–13628.
- 8 Z. Wang, C. Li and K. Domen, *Chem. Soc. Rev.*, 2019, **48**, 2109–2125.
- 9 Z. Wang, J. Peng, X. Feng, Z. Ding and Z. Li, *Catal. Sci. Technol.*, 2017, **7**, 2524–2530.
- 10 T. Hisatomi, J. Kubota and K. Domen, *Chem. Soc. Rev.*, 2014, **43**, 7520–7535.
- 11 A. Fujishima and K. Honda, *Nature*, 1972, **238**, 37–38.
- 12 H. Luo, W. Song, P. G. Hoertz, K. Hanson, R. Ghosh, S. Rangan, M. K. Brennaman, J. J. Concepcion, R. A. Binstead, R. A. Bartynski, R. Lopez and T. J. Meyer, *Chem. Mater.*, 2013, **25**, 122–131.
- 13 S. P. Adhikari, Z. D. Hood, K. L. More, I. Ivanov, L. Zhang, M. Gross and A. Lachgar, *RSC Adv.*, 2015, **5**, 54998–55005.
- 14 X. Sun, Q. Li, J. Jiang and Y. Mao, *Nanoscale*, 2014, **6**, 8769–8780.
- 15 M. Sathish, B. Viswanathan, R. P. Viswanath and C. S. Gopinath, *Chem. Mater.*, 2005, **17**, 6349–6353.
- 16 P. A. Bharad, K. Sivaranjani and C. S. Gopinath, *Nanoscale*, 2015, **7**, 11206–11215.
- 17 (a) S. Mandala, S. Adhikari, P. Shengyana, M. Huia and D. M. Kim, *Appl. Surf. Sci.*, 2019, **498**, 143840; (b) X. Liu, J. Iocozzia, Y. Wang, X. Cui, Y. Chen, S. Zhao, Z. Li and Z. Lin, *Energy Environ. Sci.*, 2017, **10**, 402–434.
- 18 X. Zhang, Z. Lai, Q. Ma and H. Zhang, *Chem. Soc. Rev.*, 2018, **47**, 3301–3338.
- 19 M. Faraji, M. Yousefi, S. Yousefzadeh, M. Zirak, N. Naseri, T. H. Jeon, W. Choi and A. Z. Moshfegh, *Energy Environ. Sci.*, 2019, **12**, 59–95.
- 20 B. B. Kale, J.-O. Baeg, S. K. Apte, R. S. Sonawane, S. D. Naik and K. R. Patil, *J. Mater. Chem.*, 2007, **17**, 4297–4303.
- 21 D. Voiry, M. Salehi, R. Silva, T. Fujita, M. Chen, T. Asefa, V. B. Shenoy, G. Eda and M. Chhowalla, *Nano Lett.*, 2013, **13**, 6222–6227.
- 22 B. Chai, T. Peng, P. Zeng and J. Mao, *J. Mater. Chem.*, 2011, **21**, 14587–14593.
- 23 Y. Hong, J. Zhang, F. Huang, J. Zhang, X. Wang, Z. Wu, Z. Lin and J. Yu, *J. Mater. Chem. A*, 2015, **3**, 13913–13919.
- 24 A. F. Shaikh, S. S. Arbuj, M. S. Tamboli, S. D. Naik, S. B. Rane and B. B. Kale, *ChemistrySelect*, 2017, **2**, 9174–9180.
- 25 B. B. Kale, J.-O. Baeg, S. M. Lee, H. Chang, S.-J. Moon and C. W. Lee, *Adv. Funct. Mater.*, 2006, **16**, 1349–1354.
- 26 S. Shen, L. Zhao and L. Guo, *Int. J. Hydrogen Energy*, 2008, **33**, 4501–4510.
- 27 S. R. Kadam, D. J. Late, R. P. Panmand, M. V. Kulkarni, L. K. Nikam, S. W. Gosavi, C. J. Park and B. B. Kale, *J. Mater. Chem. A*, 2015, **3**, 21233–21243.
- 28 (a) J. Pan, Z. Guan, J. Yang and Q. Li, *Chin. J. Catal.*, 2020, **41**, 200–208; (b) N. S. Chaudhari, A. P. Bhirud, R. S. Sonawane, L. K. Nikam, S. S. Warule, V. H. Rane and B. B. Kale, *Green Chem.*, 2011, **13**, 2500–2506.
- 29 G. Yang, D. Chen, H. Ding, J. Feng, J. Z. Zhang, Y. Zhu, S. Hamid and D. W. Bahnemann, *Appl. Catal., B*, 2017, **219**, 611–618.
- 30 J. Hou, C. Yang, H. Cheng, Z. Wang, S. Jiao and H. Zhu, *Phys. Chem. Chem. Phys.*, 2013, **15**, 15660–15668.
- 31 Y. Chen, G. Tian, W. Zhou, Y. Xiao, J. Wang, X. Zhang and H. Fu, *Nanoscale*, 2017, **9**, 5912–5921.
- 32 F. Fang, L. Chen, Y.-B. Chen and L.-M. Wu, *J. Phys. Chem. C*, 2010, **114**, 2393–2397.
- 33 L. Wang, H. Zhai, G. Jin, X. Li, C. Dong, H. Zhang, B. Yang, H. Xie and H. Sun, *Phys. Chem. Chem. Phys.*, 2017, **19**, 16576–16585.
- 34 S. B. Kale, R. S. Kalubarme, M. A. Mahadadalkar, H. S. Jadhav, A. P. Bhirud, J. D. Ambekar, C.-J. Park and B. B. Kale, *Phys. Chem. Chem. Phys.*, 2015, **17**, 31850–31861.
- 35 N. S. Chaudhari, S. S. Warule and B. B. Kale, *RSC Adv.*, 2014, **4**, 12182–12187.
- 36 M. A. Mahadik, P. S. Shinde, M. Cho and J. S. Jang, *J. Mater. Chem. A*, 2015, **3**, 23597–23606.
- 37 (a) Z. Guan, J. Pan, Q. Li, G. Li and J. Yang, *ACS Sustainable Chem. Eng.*, 2019, **7**, 7736–7742; (b) A. K. Kulkarni, Y. A. Sethi, R. P. Panmand, L. K. Nikam, J.-O. Baeg, N. R. Munirathnam, A. V. Ghule and B. B. Kale, *J. Energy Chem.*, 2017, **26**, 433–439.
- 38 W. Y. Lim, M. Hong and G. W. Ho, *Dalton Trans.*, 2016, **45**, 552–560.
- 39 X. Gao, J. Wang, J. Yu and H. Xu, *CrystEngComm*, 2015, **17**, 6328–6337.
- 40 M. A. Mahadadalkar, S. W. Gosavi and B. B. Kale, *J. Mater. Chem. A*, 2018, **6**, 16064–16073.
- 41 B. Ghosh, M. Das, P. Banerjee and S. Das, *Fabrication and optical properties of SnS thin films by SILAR method*, 2008.
- 42 L. Ye, J. Fu, Z. Xu, R. Yuan and Z. Li, *ACS Appl. Mater. Interfaces*, 2014, **6**, 3483–3490.
- 43 H. Jia, W. He, Y. Lei, X. Chen, Y. Xiang, S. Zhang, W. M. Lau and Z. Zheng, *RSC Adv.*, 2013, **3**, 8909–8914.
- 44 B. Subramanian, C. Sanjeeviraja and M. Jayachandran, *Mater. Chem. Phys.*, 2001, **71**, 40–46.
- 45 P. Gomathisankar, K. Hachisuka, H. Katsumata, T. Suzuki, K. Funasaka and S. Kaneco, *ACS Sustainable Chem. Eng.*, 2013, **1**, 982–988.
- 46 S. R. Lingampalli, U. K. Gautam and C. N. R. Rao, *Energy Environ. Sci.*, 2013, **6**, 3589–3594.
- 47 Y. A. Sethi, C. S. Praveen, R. P. Panmand, A. Ambalkar, A. K. Kulkarni, S. W. Gosavi, M. V. Kulkarni and B. B. Kale, *Catal. Sci. Technol.*, 2018, **8**, 2909–2919.
- 48 (a) S. Adhikari, A. V. Charanpahari and G. Madras, *ACS Omega*, 2017, **2**, 6926–6938; (b) S. Wang, B. Y. Guan, X. Wang and X. W. D. Lou, *J. Am. Chem. Soc.*, 2018, **140**, 15145–15148.
- 49 H. Wang, H. Ye, B. Zhang, F. Zhao and B. Zeng, *J. Phys. Chem. C*, 2018, **122**, 20329–20336.
- 50 S. Shen, X. Chen, F. Ren, C. X. Kronawitter, S. S. Mao and L. Guo, *Nanoscale Res. Lett.*, 2011, **6**, 290.
- 51 S. Jayswal and R. S. Moirangthem, *New J. Chem.*, 2018, **42**, 13689–13701.

